Segmentation of the prostate from suprapubic ultrasound images

Yongjian Yu and Janelle A. Molloy[a)]
Department of Radiation Oncology, University of Virginia, Charlottesville, Virginia 22903

Scott T. Acton
Department of Electrical and Computer Engineering, University of Virginia, Charlottesville, Virginia 22903

(Received 8 March 2004; revised 2 August 2004; accepted for publication 2 September 2004; published 23 November 2004)

We present a technique for semiautomated segmentation of human prostates using suprapubic ultrasound (US) images. In this approach, a speckle reducing anisotropic diffusion (SRAD) is applied to enhance the images and the instantaneous coefficient of variation (ICOV) is utilized for edge detection. Segmentation is accomplished via a parametric active contour model in a polar coordinate system that is tailored to the application. The algorithm initially approximates the prostate boundary in two stages. First a primary contour is detected using an elliptical model, followed by a primary contour optimization using an area-weighted mean-difference binary flow geometric snake model. The algorithm was assessed by comparing the computer-derived contours with contours produced manually by three sonographers. The proposed method has application in radiation therapy planning and delivery, as well as in automated volume measurements for ultrasonic diagnosis. The average root mean square discrepancy between computed and manual outlines is less than the inter-observer variability. Furthermore, 76% of the computer-outlined contour is less than 1 σ manual outline variance away from "true" boundary of prostate. We conclude that the methods developed herein possess acceptable agreement with manually contoured prostate boundaries and that they are potentially valuable tools for radiotherapy treatment planning and verification. © *2004 American Association of Physicists in Medicine.* [DOI: 10.1118/1.1809791]

Key words: prostate segmentation, active contour, level set, speckle reduction, instantaneous coefficient of variation

I. INTRODUCTION

Radiation therapy is accepted as a standard of care for prostate cancer, whether it is delivered externally, via conformal radiation therapy, or interstitially via implantation of radioactive seeds (brachytherapy). The high soft tissue contrast produced by ultrasound (US) imaging has made US a useful imaging modality for localization of the prostate in both cases, with transrectal ultrasound (TRUS) imaging being used in brachytherapy applications and suprapubic US imaging in external beam therapy. Two systems are commercially available for suprapubic prostate localization prior to daily radiation therapy delivery; the B-mode acquisition and targeting system (BAT™), (Nomos Corp., Sewickly, PA) and the SonArray™ (ZMed, Inc., Ashland, MA).

Contouring of the prostate is necessary for treatment planning prior to brachytherapy and may be performed in certain cases for real-time treatment planning.[1] When suprapubic US is used for daily localization of the prostate for external beam radiation therapy, the location is visualized interactively by the therapist and is not specifically contoured. Automatic contouring (or segmentation) of the prostate may prove to be useful to the degree that manual contouring is time consuming and subjective.

In this paper we focus on application of a unique method for semiautomatic segmentation of the prostate using suprapubic US images in the framework of active contour models. We derived an active contour model in a polar coordinate system and applied it to US images that were enhanced via speckle reducing anisotropic diffusion (SRAD).[2] Edge detection was facilitated by use of the instantaneous coefficient of variation (ICOV).[2,3] To reduce the sensitivity of the active contour model, we incorporated the use of region-based active contours with area-weighted binary flow as the primary optimization.[4] We assessed the algorithm performance by comparing the computer-derived contours with manually derived contours outlined by multiple sonographers. Our methodology is unique in the following aspects:

(1) Our manual initialization requires a user to select only two points near and outside the prostate volume, instead of four control points exactly on the prostate boundary as with some existing semiautomatic method.[20]
(2) The technique uses a unique primary contour optimization that incorporates a region-based, area-weighted binary flow model. This optimization is easy to implement and has high precision in boundary location.
(3) A computationally efficient polar, parametric active contour model serves as the engine for final contour optimization. Its efficiency is due to the fact that neither reparameterization nor resampling is required.
(4) In the final optimization, SRAD is used for image enhancement and speckle filtering and the ICOV is used to derive the image-based force for moving the polar active contour to the prostate boundary.

II. BACKGROUND

A number of methods have been proposed for the determination of the prostate boundary from ultrasound imagery. These methods fall into three general classes: Pixel-by-pixel classification, edge detection and linking, and deformable shape/contour models.

A. Methods based on pixel-by-pixel classification

Prater *et al.* reported an approach[6] for segmenting transrectal US images of the prostate by virtue of pixel-by-pixel classification of the prostatic and nonprostatic tissues using neural networks. The training of the networks requires extensive sets of pre-processed grayscale images and corresponding manual segmentation maps.

A texture-based classifier[7] has also been proposed for prostate segmentation, consisting of the creation of four texture-energy measure images followed by a clustering process and a probability labeling process. The drawback of these two algorithms is that they often do not result in a single, closed, contour for the prostate.

B. Methods based on edge detection and linking

The radial bas-relief (RBR)[8] method of Liu *et al.* first computes the difference between the input image and its enlargement to form an edge strength image. Then a post-processing is invoked based on morphological filtering to extract a "band-type," incomplete prostate boundary which is often connected by many spurious branches. Yet, the prostate boundary derived from this method possesses some ambiguity. Using polar coordinate Fourier transform, Kwoh *et al.* proposed a harmonic method[9] to trim the result of the RBR algorithm. However, use of the harmonic method is not possible when the RBR boundary is not a single-valued function of the polar angle.

Pathak *et al.* proposed an edge-guided interactive method[10] for prostate boundary delineation. The image contrast and speckle are initially improved via the "STICKS" algorithm and anisotropic diffusion. Then Canny's edge detector and manual edge linking are applied to form a closed contour based on *a prior* knowledge of the prostate.

Aarnink *et al.* implemented an integrated-edge-based method[11,12] for the prostate contour determination. After the input image is compressed and smoothed, the gradient and the second derivative of the image are calculated. Then, possible edges for the prostate boundary are located by zero-crossing detecting the second derivative of the image; and the edge strength assumes the value of the gradient magnitude. Finally, a post-processing is performed to extract the prostate contour based on *a prior* knowledge of the prostate in ultrasound images. However, the methodology shows a tendency to underestimate the prostate volume.

C. Methods based on deformable shape/contour models

Cosío and Davies reported the use of a point distribution model (PDM),[13] a flexible shape template, for prostate segmentation. A genetic model fitting is used to optimize a cost function that nominally corresponds to an optimal prostate shape. Though this approach always yields closed boundaries, the PDM is subjective to dependence on the selection of the training set.

Lodak *et al.* developed a semiautomatic algorithm[5] for contouring the prostate in two-dimensional (2D) ultrasound imagery based on the discrete dynamic contour model (DDC).[14] The DDC contour evolves as each vertex on the contour moves under the action of internal, external, and damping forces. Equilibrium is achieved nominally when every vertex resides on the prostate boundary. The initialization of the algorithm requires manually selecting four control points on the prostate boundary. The algorithm incorporates a tool that allows a user to edit incorrect vertices.

Wang *et al.* described a method[15] for segmenting three-dimensional (3D) ultrasound images. A 3D data set is subdivided into a sequence of evenly spaced parallel or radial 2D slices. Each slice is segmented and all segmented slices stack together to get volumetric segmentation. A fully 3D extension to the 2D DDC-based segmentation has been reported by Hu *et al.*[16]

The active contour or "snake" models of Kass *et al.*[17] are a class of energy minimization-based segmentation techniques. The basic snake model is a parametric, closed curve that evolves under the influence of internal forces, image-based external forces, and constraint forces. When an initial curve is placed close to the target boundary, the curve will evolve to fit the boundary of target. Knoll *et al.* developed a multiscale segmentation[18] algorithm for prostate TRUS scans using a snake with shape constraints. The initial contour is obtained by comparing two or three training prostate models against a rough edge map. In practice, however, to cope with wide anatomic variety in prostatic images acquired from multiple viewing angles for different patients, the set of the training models needs to be extended to contain a variety of shapes. As a result, the initialization method could become computationally expensive due to its multiscale nature.

Most snake models depend heavily on local edge information. In contrast, region-based contour models are an alternative, energy-minimizing class of models[19,20] that exploit regional information. Examples of region-based snakes are the *binary flow model*[21] by Yezzi *et al.* and the *active contours without edges* of Chan *et al.* These models excel over active contour models in cases where high image noise or low contrast precludes movement of the edge-based contour. Furthermore, region-based contours are less likely to be sensitive to the initialization of the contour, are allowed to evolve topologically and are advantageous over parametric curve segmentation in this respect. To facilitate topological changes during curve evolution, the curves in region-based models are represented implicitly by level sets. Proposed by Osher and Sethian,[22] the level set curve is computed by finding the intersection of a three-dimensional surface with the plane of zero height. Tsai *et al.* extended the region-based binary flow model to include a shape-based constraint represented by a point distribution model formulated with level

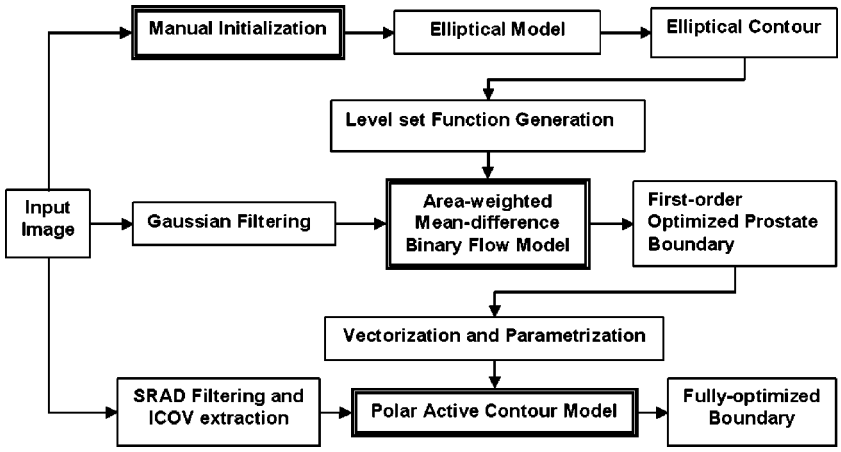

FIG. 1. Flow chart of the methodology used to delineate the prostate boundary in ultrasound imagery.

sets[23] and reported good visual results for 2D and 3D prostate contouring.

III. METHODS AND MATERIALS

Figure 1 illustrates the processing modules and data flows used in our method for semiautomated prostate segmentation. It consists of three primary modules that yield successively more accurate estimates of the prostate boundary. The manual initialization results in an elliptical contour approximation represented a level set function. This is used as input into the primary (first-order) optimization that uses an area-weighted mean-difference binary flow (AMBF) model. The resulting approximate contour is then used to initialize a polar active contour model wherein the fully optimized contour is produced.

A. Initialization

1. Manual initialization and elliptical model

The algorithm is initialized by manually selecting two points in the input US image: One near and outside the upper left part of the prostate and the other near and outside the lower right part of the prostate so that the prostate is enclosed as tightly as possibly by a reference rectangle with upper left and lower right vertices being the chosen points. This is the only user input required in the segmentation process. The objective of the primary delineation is to obtain a very general approximation of the prostate boundary location. For simplicity, we chose an ellipse as an approximation of the prostate contour. Within the reference rectangle, an inscribed elliptic contour, $\vec{C}_0$, is generated. Figures 2(a) and 2(b) show two examples of the primary delineation by the elliptic model. The bead-like markers are the points specified by user.

Ultrasound signals are high in dense media and at tissue interfaces in which the density and other acoustic properties differ. Because the prostate is surrounded by fat, muscle, and vascular tissues, acoustic reflections at these interfaces are relatively strong and create an ultrasound image that has good contrast between the differing tissues. A typical suprapubic US image is shown in Fig. 3. The bladder appears as the large anechoic (i.e., black) region due to the lack of acoustic reflection in the urine, and the smaller circular re-

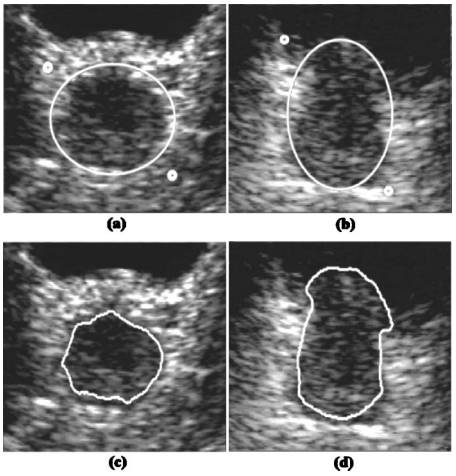

FIG. 2. The manual initialization and resulting elliptical model are shown for two prostates in (a) and (b). The manual initialization points are shown by bead-like markers. In (c) and (d) we display the result of applying the AMBF model to obtain a primary approximation to the prostate boundary.

FIG. 3. A full size test suprapubic US image wherein the bladder and the prostate can be seen.

gion inferior to the bladder is the prostate. The instantaneous coefficient of variation employed in our algorithm finds the physical interfaces of adjacent tissues.

B. Primary optimization

The objective of the primary optimization is to move the initial elliptical contour closer to the prostate boundary location in a computationally efficient manner. Since the prostate boundary appears noisy and often discontinuous in ultrasound image suffering from speckle, region-based active contours are well suited for this purpose for their insensitivity to local edge information and initialization. However, they typically require a weighted curvature term to prevent the contour from evolving into nonanatomical shapes due to the presence of noise. Use of this term is undesirable because an application-specific weight parameter has to be incorporated into the model and it requires a complex implicit discretization scheme. The use of the curvature term may be avoided by smoothing the input image, although this can produce a position bias. We therefore derived a new model that overcomes these problems.

1. Area-weighted mean-difference binary flow model (AMBF)

The AMBF model is a region-based active contour that does not depend on image edge features. It is derived by minimizing the following cost functional

$$E(\vec{C}) = -\frac{1}{2}\frac{A_u A_v}{A}(u-v)^2, \tag{1}$$

of a closed curve $\vec{C}$, where A_u and A_v are, respectively, the areas of the regions inside and outside the curve $\vec{C}$; $A=A_u+A_v$, the area of the image; u and v are the means of the Gaussian-filtered image $\tilde{I}_g$ inside and outside the curve $\vec{C}$, respectively. $\tilde{I}_g = I \otimes g_\sigma$ is the convolution of the input image I and a 2D Gaussian kernel g_σ having a standard deviation σ. Filtering at an empirically derived standard deviation of 4 allows us to preserve the prostate edges while minimizing noise and producing an anatomically appropriate contour.

Using a level set representation and the regularization method of Chan and Vese[19] we find that the segmenting curve $\vec{C}$ is the zero-level set of a function $\phi(x,y;t\to\infty)$ that is a steady state solution to the following partial differential equation:

$$\begin{cases} \dfrac{\partial \phi}{\partial t} = \delta_\varepsilon(\phi)\dfrac{1}{A}(u-v)\left[A_v(\tilde{I}_g-u)+A_u(\tilde{I}_g-v) - \dfrac{1}{2}(A_u-A_v)(u-v)\right], \\ \phi(x,y;0)=\phi_0(x,y) \quad in\ \Omega, \\ \delta_\varepsilon(\phi)\dfrac{\partial \phi}{\partial \vec{n}} = 0 \quad on\ \partial\Omega, \end{cases} \tag{2}$$

where

$$A_u = \int\int_\Omega H_\varepsilon(\phi(x,y))dxdy, \tag{3}$$

$$A_v = \int\int_\Omega [1-H_\varepsilon(\phi(x,y))]dxdy, \tag{4}$$

$$u = (1/A_u)\int\int_\Omega \tilde{I}_g(x,y)H_\varepsilon(\phi(x,y))dxdy, \tag{5}$$

$$v = (1/A_v)\int\int_\Omega \tilde{I}_g(x,y)[1-H_\varepsilon(\phi(x,y))]dxdy, \tag{6}$$

$H_\varepsilon(z)=\frac{1}{2}[1+(2/\pi)\arctan(z/\varepsilon)]$ (i.e., the regularized Heaviside function[19]), $\delta_\varepsilon(z)=dH_\varepsilon(z)/dz$ (i.e., the regularized Dirac function[19]), ε is a small parameter; Ω and $\partial\Omega$ are, respectively, the image domain and its boundary, $\vec{n}$ denotes the exterior normal to $\partial\Omega$, $\partial\phi/\partial\vec{n}$ denotes the normal derivative of ϕ on $\partial\Omega$.

The partial differential equation (2) is solved numerically using a Jacobi iterative method. Choosing a sufficiently small time step Δt and a grid size h in both x and y directions, we discretize the time and space coordinates as: $t=n\Delta t$, $(n=0,1,\ldots)$, $x=ih$, $y=jh$, $(i=0,1,\ldots,M-1$, $j=0,1,2,\ldots,N-1)$, where $Mh\times Nh$ is the area of the image domain. Let $\tilde{I}_{g,i,j}=\tilde{I}_g(ih,jh)$ and $\phi^n_{i,j}=\phi(ih,jh;n\Delta t)$. The algorithm is as follows: Knowing ϕ^n, we first compute $A_u(\phi^n)$, $A_v(\phi^n)$, $u(\phi^n)$ and $v(\phi^n)$ using (3)–(6), respectively. Then, we compute ϕ^{n+1} using the following update equation system

$$\begin{aligned}\frac{\phi^{n+1}_{i,j}-\phi^n_{i,j}}{\Delta t} = \delta_h(\phi^n_{i,j})\frac{1}{A}&[u(\phi^n)-v(\phi^n)]\{A_v(\phi^n)[\tilde{I}_{g,i,j}-u(\phi^n)] \\ &+A_u(\phi^n)[\tilde{I}_{g,i,j}-v(\phi^n)]-(1/2) \\ &\times[A_u(\phi^n)-A_v(\phi^n)][u(\phi^n)-v(\phi^n)]\}.\end{aligned} \tag{7}$$

The initial level set function is set to

$$\phi^0_{i,j} = h\sqrt{(i-\mathrm{round}(x_c/h))^2 + a^2/b^2(j-\mathrm{round}(y_c/h))^2} - a, \tag{8}$$

where a, b, x_c, and y_c are the two half (major/minor) axes and the center coordinates of the initial elliptical contour, respectively, and round(x) indicates rounding x to the nearest integer. We used the model parameters: $h=1$, $\Delta t=0.1$, and $\sigma=4$. As the first-order optimizer, the update equation (7) does not proceed until convergence is reached but stops when the area of the region inside the contour differs from that of the initial ellipse by 20%. This stopping criterion was determined empirically and allows the contour to move to sufficiently close to the prostate boundary while preventing erroneous small contours from emerging.

From the resulting level set function, $\phi(x,y)$, the primary optimal contour is obtained by

$$C = \{(x,y) \in \Omega | \phi(x,y) = 0\}. \quad (9)$$

Figures 2(c) and 2(d) show the two examples of the primary contour optimization, initialized by the ellipses shown in Figs. 2(a) and 2(b), respectively. For the primary optimization, the AMBF fully employs the observation that the majority of the prostate appears hypoechoic relative to the echo pattern of the neighboring normal tissues.

2. Vectorization of binary contour

Since the AMBF model[4] produces only a binary contour mask, we must produce the required vectorized curve $\boldsymbol{\rho}^0 = [\rho_0(\theta_0)\rho_0(\theta_1)\cdots\rho_0(\theta_{N-1})]^T$ for input into the full optimization module. Initially, an edge-tracing algorithm is applied to the binary contour mask to obtain an ordered sequence of the Cartesian coordinates $\{(x_j,y_j)|j=1,2,\ldots,M\}$ for all contour pixels. The Cartesian coordinates of these pixels are then transformed into polar coordinates $\{(r_j,\varphi_j)|j=1,2,\cdots,M\}$ by $r_j=\sqrt{(x_j-x_c)^2+(y_j-y_c)^2}$ and $\varphi_j=\arctan(y_j-y_c/x_j-x_c)$ with $0\leqslant\varphi_j\leqslant 360°$, where the polar coordinate system is centered at $x_c=(1/M)\Sigma_{j=1}^{M}x_j$ and $y_c=(1/M)\Sigma_{j=1}^{M}y_j$. The sequence is then sorted such that it is properly aligned with the first element possessing the least polar angle and the last one possessing the largest polar angle. Finally, the sequence is evenly sampled in the angular direction through linear interpolation to obtain the $\boldsymbol{\rho}^0=[\rho_0(\theta_0)\rho_0(\theta_1)\cdots\rho_0(\theta_{N-1})]^T$.

C. Final optimization

Once an approximation of the prostate boundary has been made through manual initialization and primary optimization, the algorithm proceeds to further optimize the contour by matching it to the prostate boundary location and smoothing it. To this end, use of local edge information and boundary smoothness constraint becomes essential in order to segment an anatomically realistic boundary. The optimization method we derived is a parametric, polar active contour model dedicated to convex, closed shapes that are assumed by most prostates. To effectively distinguish prostate edges from the speckle-induced phantom edges, the image features used to attract the contour are measured by the ICOV[2,3] edge strength computed from an SRAD[2,3] processed input image (see Appendices A and B for a brief description of ICOV and SRAD). In the following, we describe the polar active contour model and its numerical implementation.

1. Polar active contour model

Traditional active contours[17,24] are typically formulated in rectangular coordinate systems. Since the prostate is convex in the axial trans-abdominal US images, we developed an active contour model in a polar coordinate system (ρ,θ) whose origin O' is near the center of the prostate. This polar model renders approximately 50% reduction in the algorithm complexity compared with rectangular snakes (see Sec. V).

The relationship between the Cartesian coordinate system $(x\text{-}o\text{-}y)$ and the polar coordinate system $(\rho\text{-}\theta\text{-}O')$ is illustrated in Fig. 4. $\vec{R}_c$ denotes the position vector of point O',

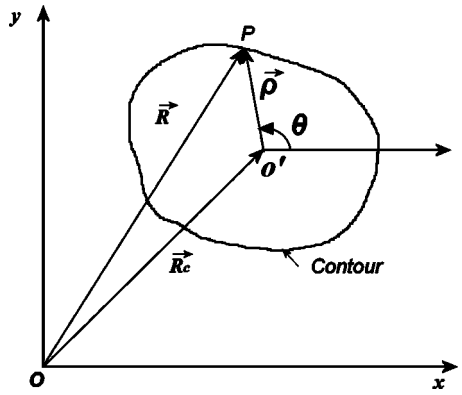

FIG. 4. Geometry of the polar coordinate system.

the origin of the polar coordinate system, in the Cartesian system. $\vec{R}$ and $\vec{\rho}$ represents, respectively, the position vectors of a point P on the contour in the Cartesian system and the polar system. In the polar coordinate system, we define a radial segmenting curve $\rho=\rho(\theta), \theta\in[0,2\pi]$, that minimizes the following energy functional:

$$E(\rho) = \int_0^{2\pi} \{(\alpha(\theta)/2)[\rho'(\theta)]^2 + (\beta(\theta)/2)[\rho''(\theta)]^2 + E_{\text{ext}}(\vec{R}_c + \rho(\theta)\hat{e}_\rho)\}d\theta, \quad (10)$$

where α and β are parameters that impose the elasticity and rigidity of the snake, respectively, and $\rho'(\theta)$ and $\rho''(\theta)$ denote the first and second derivatives of the curve $\rho(\theta)$ with respect to angle θ. The external energy function E_{ext} is derived from the input image I as the negative value of a particular edge strength measure called ICOV so that it takes on smaller values near structure boundaries. $\hat{e}_\rho=\hat{e}_x\cos\theta+\hat{e}_y\sin\theta$ where $\hat{e}_x$ and $\hat{e}_y$ are unit vectors in the x and y direction, respectively. Using the calculus of variations, we find that an active contour that minimizes (10) should satisfy the Euler equation:

$$\frac{d}{d\theta}[\alpha(\theta)\rho'(\theta)] - \frac{d^2}{d\theta^2}[\beta(\theta)\rho''(\theta)] - \frac{\partial E_{\text{ext}}}{\partial \rho} = 0. \quad (11)$$

The first two terms in (11) comprise the contour internal (i.e., smoothing) forces, while the last term represents the external image-based force that moves the contour toward the image edges.

The solution to (11) is determined by treating ρ as a function of time t as well as θ. Then the partial derivative of ρ with respect to t is set equal to the left-hand side of (11), yielding

$$\dot{\rho}(\theta,t) = \frac{\partial}{\partial\theta}[\alpha(\theta)\rho'(\theta,t)] - \frac{\partial^2}{\partial\theta^2}[\beta(\theta)\rho''(\theta,t)] - \frac{\partial E_{\text{ext}}}{\partial\rho}, \quad (12)$$

where $\dot{\rho}=\partial\rho/\partial t$, and $\rho(\theta,t=0)=\rho_0(\theta)$. To compute the partial derivative of E_{ext}, which is given in the Cartesian coordinate system we use the chain rule to obtain

$$\frac{\partial E_{\text{ext}}}{\partial \rho} = \cos(\theta)\frac{\partial E_{\text{ext}}}{\partial x} + \sin(\theta)\frac{\partial E_{\text{ext}}}{\partial y}. \tag{13}$$

In a traditional parametric active contour,[17,24] the external image-based energy for grayscale imagery is designed as

$$E_{\text{ext}}(x,y) = -\| \nabla [\tilde{I}_g(x,y)]\|^2, \tag{14}$$

where $\tilde{I}_g(x,y)$ is the Gaussian filtered gray-scale value of the input image I. For ultrasound imagery, however, Gaussian filtering and gradient edge detection are not suitable due to the presence of signal-dependent speckle noise. We, therefore, chose to use SRAD as our filter and the ICOV edge detector. Further, we propose that the external energy be defined as the negative value of the ICOV edge strength

$$E_{\text{ext}}(x,y) = -\frac{|(1/2)\| \nabla \tilde{I}_s\|^2 - (1/16)(\nabla^2 \tilde{I}_s)^2|}{[\tilde{I}_s + (1/4)\nabla^2 \tilde{I}_s]^2}, \tag{15}$$

where $\tilde{I}_s$ is the SRAD-filtered, echo intensity image I_d. SRAD requires the echo signal intensity as its input. However, the available B-scan image is the log-compressed version of the echo intensity image. Therefore, B-scan data must be decompressed to recover an estimate of the echo intensity in order to be processed via SRAD. To do this, we simply took $I_d = \exp(I/D)$, the exponential of the B-scan data divided by a constant D. Then we chose a value of D such that the speckle statistics of the decompressed image mimics the theoretical statistics of intensity of fully developed speckle (see Appendix C). Empirically, we found that $D=25$ (unit: the reciprocal of the logarithm of I_d since I is dimensionless) for the US imagery used.

2. Numerical implementation

Equation (12) is a general formulation of the parametric polar active contour model in which two model parameters are allowed to vary with angle. In practice, however, α is usually set to a positive constant and β is usually zero. Using these assumptions, Eq. (12) is implemented as follows. First select a time step size Δt and an angle increment of h to quantize the time variable and the angle variable as: $t = n\Delta t$, $(n = 0,1,2,\ldots)$ and $\theta = ih$, $(i = 0,1,2,\ldots,N-1)$, where $h = 2\pi/N$. Let $\theta_i = ih$ and $\rho_i^n = \rho(ih, n\Delta t)$ be an approximation of $\rho(\theta,t)$. The external force can then be made discrete in the radial direction $-\partial E_{\text{ext}}/\partial \rho$ as follows:

$$F_i^n = -\left[\cos\theta_i \frac{\partial E_{\text{ext}}}{\partial x} + \sin\theta_i \frac{\partial E_{\text{ext}}}{\partial y}\right]\Bigg|_{x_c+\rho_i^n\cos\theta_i,\, y_c+\rho_i^n\sin\theta_i}, \tag{16}$$

where x_c and y_c are the Cartesian coordinates of the origin of the polar coordinate system. If the origin of the Cartesian coordinate system is at the upper left corner of the image, we approximate (12) using

$$\frac{\rho_i^{n+1} - \rho_i^n}{\Delta t} = \frac{\alpha}{h^2}[\rho_{i\oplus 1}^n - 2\rho_i^n + \rho_{i\Theta 1}^n] - \frac{\beta}{h^4}[(\rho_{i\oplus 2}^n - 2\rho_{i\oplus 1}^n + \rho_i^n) - 2(\rho_{i\oplus 1}^n - 2\rho_i^n + \rho_{i\Theta 1}^n) + (\rho_i^n - 2\rho_{i\Theta 1}^n + \rho_{i\Theta 2}^n)] + F_i^n, \tag{17}$$

where $\oplus$ and Θ are modulo N addition and subtraction, respectively. The difference equations (17) can be written in the following matrix form:

$$\boldsymbol{\rho}^{n+1} = \boldsymbol{\rho}^n - \boldsymbol{A}\boldsymbol{\rho}^n\Delta t + \boldsymbol{F}\Delta t, \tag{18}$$

where

$$\boldsymbol{\rho}^n = \begin{bmatrix} \rho_0^n \\ \rho_1^n \\ \vdots \\ \rho_{N-1}^n \end{bmatrix}, \quad \boldsymbol{F} = \begin{bmatrix} F_0^n \\ F_1^n \\ \vdots \\ F_{N-1}^n \end{bmatrix},$$

and

$$\boldsymbol{A} = \begin{bmatrix} c & b & a & & & a & b \\ b & c & b & a & & & a \\ a & b & c & b & a & & \\ & & & \ddots & & & \\ & & a & b & c & b & a \\ a & & & a & b & c & b \\ b & a & & & a & b & c \end{bmatrix}$$

being a $N \times N$ symmetric pentadiagonal matrix with $a = \beta/h^4$, $b = -(4\beta/h^4 + \alpha/h^2)$, and $c = 6\beta/h^4 + 2\alpha/h^2$. Equation (18) is an explicit update equation that requires a sufficiently small time step for obtaining a stable numerical solution and is usually very slow to converge. For the sake of numerical stability when the time step $\Delta t = 1$ is used, an implicit update equation can be formulated as

$$\boldsymbol{\rho}^{n+1} = \boldsymbol{\rho}^n - \boldsymbol{A}\boldsymbol{\rho}^{n+1} + \boldsymbol{F} \quad \text{or} \quad \boldsymbol{\rho}^{n+1} = (\boldsymbol{I} + \boldsymbol{A})^{-1}(\boldsymbol{\rho}^n + \boldsymbol{F}), \tag{19}$$

where $\boldsymbol{I}$ is the identity matrix. Given an initial contour $\boldsymbol{\rho}^0 = [\rho_0(\theta_0)\rho_0(\theta_1)\cdots\rho_0(\theta_{N-1})]^T$, Eq. (19) is iterated until the maximum of the absolute values of the differences of two consecutive solutions is smaller than a predefined value. In this implementation, we set $\Delta t = 1$, $N = 72$, and $\beta = 0$. As for the determination of α parameter, we utilized the following approach. Assuming that the segmenting contour $\rho(\theta)$ has been found, we know that $\alpha(\theta)$ satisfies the following Euler equation

$$\frac{d}{d\theta}[\alpha(\theta)\rho'(\theta)] = \frac{\partial E(\rho(\theta),\theta)}{\partial \rho}, \tag{20}$$

under the condition that $\beta(\theta) \equiv 0$. Denoting $f(\theta) = \partial E(\rho(\theta),\theta)/\partial\rho$, $p(\theta) = \rho''(\theta)/\rho'(\theta)$ and $q(\theta) = f(\theta)/\rho'(\theta)$, we can rewrite (20) as

$$\alpha'(\theta) + \alpha(\theta)p(\theta) = q(\theta), \tag{21}$$

which is a first-order ordinary differential equation with a solution

$$\alpha(\theta) = \frac{\int_0^{\theta}\{\exp[\int_0^u p(v)dv]\}q(u)du}{\exp[\int_0^{\theta}\exp[p(u)]du]}. \quad (22)$$

We have dropped the arbitrary integration constant in the numerator of (22). In practice, the segmenting curve cannot be solved until parameter $\alpha(\theta)$ is known. We therefore used the first-order optimized contour for this purpose, assuming that the final contour is near to this. The constant elasticity parameter used in our numerical update Eq. (19) is then taken as the average of (22) over all possible angles.

D. Experimental evaluation of the segmentation algorithm

We validated our methodology by comparing semiautomatically segmented prostate contours to those determined manually by three trained sonographers. Manual outlining was accomplished using a commercial graphics software package (Paintshop™, JASC, Inc.). The segmented regions were interpreted as the prostate by radiologists and sonographers at our institution. The images were acquired as part of the patients' clinical management of prostate cancer, which included acquisition of CT scans of the region, followed by spatial registration of the US images with CT-derived contours of the prostate boundary. This registration was performed using our Department's BAT (Nomos Corp., Sewickly, PA) US system. As such, confidence that the segmented hypoechoic region indicated the prostate gland is very high.

The resulting manual segmentations were binary images, with each pixel representing either the contour or not. Since the computer-derived contours were described in a polar coordinate system, it was necessary that we transform the manual contours into the same polar coordinate system. We choose a common polar coordinate system whose origin was located at the average of the centers of mass of all of the manual contours. We then converted the binary manual contours into a vectorized form in the same manner as described in Sec. III B 2. The average manual contour for a given prostate image is given by $\overline{\boldsymbol{\rho}}=(1/K)\Sigma_{i=1}^{K}\boldsymbol{\rho}_i$ where $\boldsymbol{\rho}_i=[\rho_{i0},\rho_{i1},\ldots,\rho_{i,N-1}]^T$ is the vectorized prostate boundary segmented by the ith observer and K is the number of observers (i.e., $K=3$). The interobserver variability of the manual contours is given by the standard deviation, $\boldsymbol{\sigma}=[\sigma_0,\sigma_1,\cdots,\sigma_{N-1}]^T$ where $\sigma_j=[(1/K)\Sigma_{i=1}^{K}(\rho_{ij}-\overline{\rho_j})^2]^{1/2}$. Statistically, $\overline{\boldsymbol{\rho}}$ and $\boldsymbol{\sigma}$ characterize the center and the spread of the partially overlaid boundaries outlined by multiple observers, respectively. The region between contours $\overline{\boldsymbol{\rho}}-\boldsymbol{\sigma}$ and $\overline{\boldsymbol{\rho}}+\boldsymbol{\sigma}$ forms a band of varying width that centers the mean manually derived contour, which we will refer to as the 1 σ manual outline variance band or the 1 σ band for short.

We used three types of metrics to evaluate the performance of the proposed segmentation algorithm. (1) The root mean square error (RMSE) in distance between the computer-derived contour and the average manual contour, given by $\mathrm{RMSE}=\sqrt{(1/N)\Sigma_{j=0}^{N-1}(\hat{\rho}(\theta_j)-\overline{\rho_j})^2}$ where $\{\hat{\rho}(\theta_j)|j=0,1,2,\ldots,N-1\}$ denotes a vectorized, computer-derived boundary. (2) The errors in estimates between the manual and computer-derived areas, including fractional area difference (FAD), fractional false positive (FFP), fractional false negative (FFN), and fractional true positive (FTP) areas.[5] Let R_m and R_c be the regions enclosed by the mean manual outline and computer-derived outline, respectively; and denote the area of region R by $A(R)$. By definition, we have that $\mathrm{FAD}=|A(R_c)-A(R_m)|/A(R_m)$, $\mathrm{FFP}=|A(R_c\cup R_m)-A(R_m)|/A(R_m)$, $\mathrm{FFN}=|A(R_c\cup R_m)-A(R_c)|/A(R_m)$ and $\mathrm{FTP}=|A(R_c\cap R_m)|/A(R_m)$. (3) The 1σ-band snaxel ratio, defined as the ratio of the number of computer-derived boundary points that are located in the 1 σ band to the total number of boundary pixels, N. This metric is intended to indicate the accuracy of the computer-derived boundary relative to the manual segmentation.

The US unit used for collecting test images was a Diasonics model 100-02816-00 with a 4.0/50 curved linear array probe operated at 3.5 MHz. The ultrasound was performed with a patient lying on a couch. The ultrasound probe was scanned on the patient's abdomen in two dimensions to allow a sonographer to see the prostate in two different planes. Either a transverse (horizontal) or sagital (vertical) ultrasound image was captured and displayed on a computer screen. The frame acquired from the ultrasound equipment was then digitized and transformed into a 640×480 bitmap array quantified on 256 gray levels. Our trial data set consists of 27 axial, trans-abdominal US images from six patients. When selecting test images, we followed a subjective criterion regarding the quality of image: Test image should be manually segmented with reasonable interobserver variabil-

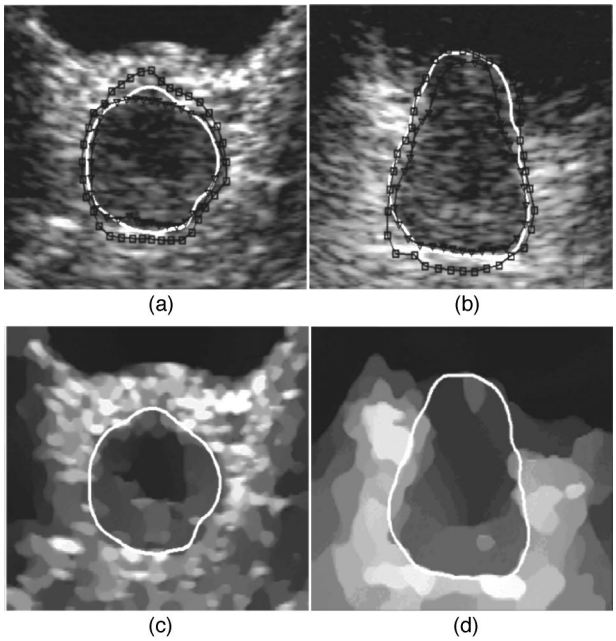

FIG. 5. Prostate segmentation by the polar ICOV snake. The white contours in (a) and (b) are the computer-derived segmentation. The region between the square and triangle marked curves corresponds to the 1 σ manual outline variance around the mean of manual outlines. (c) and (d) show the computer segmentation overlaid on the SRAD processed images, corresponding to (a) and (b), respectively.

TABLE I. Quantitative performance of the proposed method. Snaxel ratio refers to the fraction of contour points inside the 1-standard deviation and 2-standard deviation error margins, based on the manual segmentation results.

Image No.	Interobserver (AIOV) (mm)	RMSE (mm)	FAD (%)	FFP (%)	FFN (%)	FTP (%)	Snaxel ratio (1σ)
1	0.64	0.89	3.6	3.6	11.1	89.1	0.59
2	0.86	0.9	14.6	1.9	16.7	83.6	0.68
3	0.92	0.93	9	6.7	3.1	97.1	0.76
4	0.98	0.75	5.2	7.6	2.2	97.9	0.7
5	0.99	0.89	1.2	4.4	5.6	94.6	0.68
6	1	1.29	17.3	18.9	1.3	98.7	0.68
7	1.03	0.95	0.3	7.9	8.2	92	0.7
8	1.05	1.94	4.4	4.9	9.4	90.8	0.43
9	1.08	0.89	9.9	0.5	10.7	89.7	0.76
10	1.09	1.44	6	2.6	8.7	91.5	0.37
11	1.13	1.36	3.7	12.7	3.5	96.6	0.46
12	1.17	2.09	12.7	1.5	14.3	85.9	0.32
13	1.19	1.15	5.3	2.8	8.3	91.9	0.81
14	1.2	0.87	0.1	5.4	5.5	94.6	0.65
15	1.22	0.77	2.4	6.9	4.3	95.8	0.95
16	1.23	1.3	3.8	3.5	7.4	92.7	0.57
17	1.26	0.92	3.7	4.1	7.8	92.3	0.76
18	1.27	0.84	7.7	1.2	9.2	91.1	0.86
19	1.29	0.58	2.7	8.3	5.5	94.6	0.86
20	1.55	0.89	4.2	10.3	6.1	94	0.81
21	1.59	1.9	8.4	11.6	3.2	96.9	0.51
22	1.72	0.98	4.9	8.5	3.6	96.6	0.7
23	1.87	1.37	5	6	10.9	89.2	0.84
24	2.15	0.8	4.4	5.4	9.8	90.4	0.97
25	2.19	1.71	0.8	6.8	6	94.1	0.86
26	2.23	1.25	6.3	8.2	14.6	85.6	0.84
27	3.34	1.65	10.3	3.7	14.1	86.1	0.95
Ave.	1.38	1.16	5.8	6.1	7.8	92.3	0.71
Std.	0.57	0.41	4.3	4.0	4.1	4.0	0.18

ity, because it is impossible to make a reliable evaluation of the computer-derived contouring unless reliable ground truth data can be made available.

IV. RESULTS

Figure 5 shows the segmentation results from two example images (the same ones previously used to illustrate the manual initialization and primary contour optimization) with the proposed method. In Figs. 5(a) and 5(b) the contours $\boldsymbol{\rho} \pm \boldsymbol{\sigma}$, which correspond to the 1σ manual outline variance around the average (or mean) of manually outlined contour $\boldsymbol{\rho}$, and are also shown for the comparison of the result of the proposed method with manual outlining. Figures 5(c) and 5(d) illustrate the computer-delineated contours superimposed on the SRAD processed images.

Table I summarizes the quantitative comparison of the computer based method and the manual segmentation. The first column of the table numbers images and the second column lists the average inter-observer variability (AIOV) of the segmentations of multiple observers, which is defined by $\mathrm{AIOV}=\{(1/KN)\Sigma_{i=1}^{K}\Sigma_{j=1}^{N}[\rho_{ij}-\overline{\rho_j}]^2\}^{1/2}$. The AIOV serves as a natural, subjective measure of the quality of image: The poorer the image quality, the more discrepancy in manual segmentation of the prostate will occur, resulting in a larger AIOV value. As can be seen, the images sorted in ascending order of their AIOV values, meaning that image numbered small are of higher quality than those numbered big. The third column indicates the RMSE of the computer-extracted prostate contour with the ground truth being the mean of the manual segmentations. Note that the root mean square discrepancy between the computed contour and the mean of the manual contours is less than the interobserver variability, or AIOV, on average. To better appreciate the table, we plotted the AIOV and RMSE for all test images, as shown in Fig. 6. From this plot we see that the distance metric is relatively insensitive to the image quality measured by the AIOV. The fourth to seventh column of Table I give the fraction area difference, false positive, false negative and true positive areas. By plotting a bar chart, Fig. 7, with these data, it is easy to see that the FTP are greater than 80% for all images, and both FFP and FFN are less than 20%. Statistically, we have obtained an average value of 92.3% with a standard deviation of 4.0% for FTP, compared with a mean sensitivity (C_s, equal to FTP) of 94.5% with a 2.7% standard deviation re-

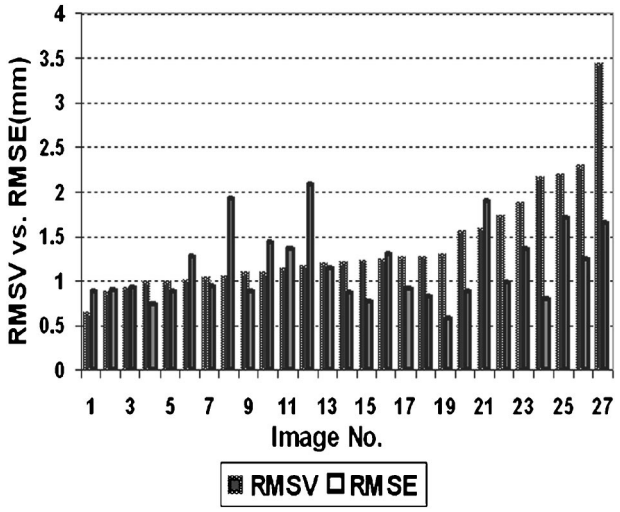

FIG. 6. Bar plot of AIOV and RMSE, showing the performance of the algorithm segmentation in images of different quality. The images are numbered in order of ascending AIOV or of descending image quality. From the plot we see that the performance of the algorithm in terms of distance metric is insensitive to the image quality within a range.

ported by Ladak *et al.*[5] In the work, Ladak *et al.* reported a mean accuracy (C_a) of 90.1% with a 3.2% standard deviation. Since $C_a = 1 - (\mathrm{FFP} + \mathrm{FFN})$, our results have an equivalent average value of C_a of 86.1% and a standard deviation 5.6%. In terms of area error metrics, our results are very close to those of Ladak *et al.*, considering the fact that they have an extra editing process in their method. The eighth columns in Table I list the snaxel ratio of the number of snake points (or "snaxels") inside the $1\,\sigma$ band. On average 76% of the computer generated contour is less than $1\,\sigma$ manual outline variance away from average manually derived boundary.

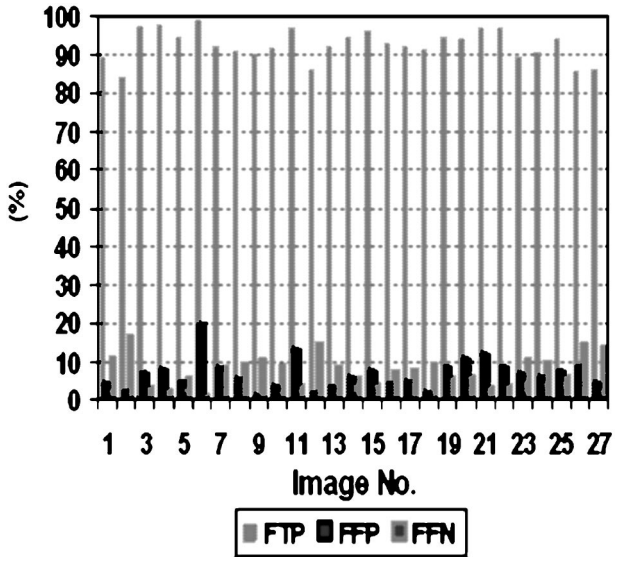

FIG. 7. Bar chart of area error metrics showing that the fractional true positive area are greater than 80% for all images, and both fractional false positive area and false negative area fractions are less than 20%.

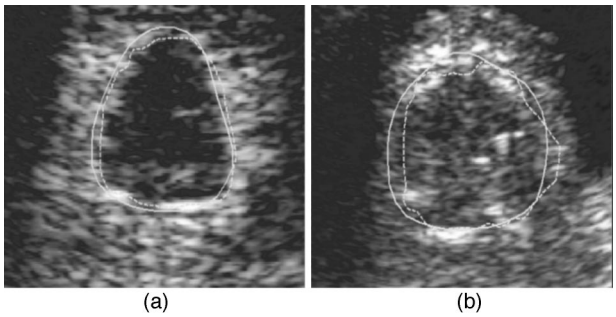

FIG. 8. Comparison of the manual mean and the computer-derived prostate segmentation on the best image (a) (image no. 1 in Table I) and the worst image (b) (image no. 27 in Table 27) in terms of AIOV value. The manual contours are solid; the dashed contours are computer-derived.

For an overall, visual assessment of the performance of the algorithm, we plotted the manually-outlined mean prostate boundary and the computer-derived boundaries from the best image (#1 in Table I) and the worst (#27 in Table I), shown in Fig. 8. The prostate boundary delineated on images of intermediate quality can be seen in Fig. 5 where the left and right column images are numbered 9 and 15 in Table I, respectively. We believe that Figs. 5 and 8 would allow a reader to make an independent, overall assessment of the performance of the algorithm and to better appreciate the meaning of the quantification in Table I.

The segmentation algorithm was implemented in MATLAB (Mathworks, Natick, MA) and achieved a processing rate of less than 7.5 s for a 128×128-pixels image on a PC with a Pentium 4 (2.6 GHz) processor, specifically it takes approximately 2.5 s to compute the first-order optimized contour, slightly less than 2 s to execute the polar snake refinement and 3 s to extract an ICOV edge image. The amount of time spent on manual initialization was not included because it varies from user to user.

V. DISCUSSION

A. Advantages of polar active contour model

One advantage of the polar active snake model for prostate segmentation is its efficiency. Consider that a conventional parametric snake requires two update equations in the form of (19) that govern the $\boldsymbol{x}$ and $\boldsymbol{y}$ coordinates of the evolving contour. Throughout the iteration process, the matrix $\boldsymbol{A}$ changes frequently because the number of snake points is allowed to vary in order to prevent the maximum distance between two adjacent points from exceeding a pre-specified limit. The conventional parametric snake is inherently slow due to the frequent matrix inversions $(\boldsymbol{I}+\boldsymbol{A})^{-1}$. These inversions can be computationally expensive if the object boundary is large. The number of computations is increased further by the fact that updates of $\boldsymbol{x}$ and $\boldsymbol{y}$ require multiplications with all elements of the matrix $(\boldsymbol{I}+\boldsymbol{A})^{-1}$ and that the evolving contour needs to be re-parameterized often. In contrast, the polar snake model does not require re-parameterization because the number of snake points N is fixed. The computation of the matrix inverse $(\boldsymbol{I}+\boldsymbol{A})^{-1}$ is performed only once

and there exists only one update equation. These properties of the polar snake model decrease the computational cost approximately by half.

B. Constant elasticity α versus angle-dependent elasticity $\alpha(\theta)$

In this paper, we assumed a constant elasticity for the polar active contours. In some applications, we deal with the segmentation of the prostate in the presence of wide, blurred edge gaps along its boundary. Thanks to its region-based AMBF model, the primarily optimized contour establishes the segment of boundary corresponding to the blurred edges to acceptable satisfaction. In the final optimization, however, while the active contour evolves to converge to definable edges, the portion of the contour bridging those wide edge gaps might be dragged away from correct positions due to the elasticity force of the contour. This problem could be solved by the use of an angle-dependent elasticity function $\alpha(\theta)$ such that the values of $\alpha(\theta)$ are equal to zero in sectors spanning wide edge gaps. It could be worth while to develop more advanced algorithm that exploits nonuniform $\alpha(\theta)$ in the follow-on work.

C. Application limitation

Our algorithm was designed on the premise that the prostate appears differently (either hypoechoic or hyperechic) relative to the echo pattern of the neighboring normal tissues, which are basically true in most cases.[25] Anatomically, the prostate is composed of three zones called the peripheral zone (PZ), the central zone (CZ), and the transition zone (TZ). The normal CZ and PZ exhibit homogeneous light- to medium-gray scale and the TZ appears moderately heterogeneously hypoechoic. Because of reflection and reverberation, the thick muscular bladder wall is generally rather echogenic, appearing bright on ultrasound images. Due to their predominantly adipose composition, the periprostatic tissues are generally quite echogenic. These image features aid in delineating the boundary of the prostate. When selecting test images, we used a subjective criterion regarding the quality of image such that each test image could be manually segmented with reasonable interobserver variability. Our algorithm is able to detect and enhance differences in image contrast while preserving and enhancing edge features. Thus, while our edge enhancement facilitates segmentation in noisy images, we still require some reasonable degree of contrast between adjacent tissues.

VI. CONCLUSIONS

We have presented a method for semiautomatic segmentation of the prostate from transabdominal ultrasound images that incorporates SRAD filtration and the ICOV edge detector. A unique polar active contour model was developed in order to reduce the computational complexity and render the algorithm significantly more efficient than that using a conventional active contour model. Verification of the method was achieved by comparison to manual segmentations. The computed segmentations agreed with the manual segmentations to within 2 mm in distance error and to 10.3% in area estimate error on average, and 76% of the computed outlines fell to within one standard deviation of the manual outlines. We conclude that the method is sufficiently accurate and efficient to make it a potentially valuable tool when used for radiation therapy treatment planning and delivery verification.

ACKNOWLEDGMENTS

This work was supported by gifts from the Dean of the School of Medicine, University of Virginia, the American Cancer Society (Grant No. IRG81-001-17), the Mellon Prostate Cancer Research Institute, and the U.S. Army Medical Research and Materiel Command. The authors would also like to thank Laurence Watson, Mario Oikonomides and Cindy Berdon for assistance with the manual segmentations.

APPENDIX A: INSTANTANEOUS COEFFICIENT OF VARIATION (ICOV)

The instantaneous coefficient of variation (ICOV) is essentially a localized measurement of the coefficient of variation that can be incorporated into an anisotropic diffusion partial differential equation (PDE). Let $I(\mathbf{x})$ represent the observed echo intensity at location $\mathbf{x}=(x,y)$ in a 2D coordinate system. The ICOV is defined by

$$q(\mathbf{x}) = \frac{|(1/2)\|\nabla I(\mathbf{x})\|^2 - (1/16)[\nabla^2 I(\mathbf{x})]^2|^{1/2}}{[I + (1/4)\nabla^2 I(\mathbf{x})]},$$

where ∇ is the gradient operator, ∇^2 the Laplacian operator, $\|\cdot\|$ the magnitude of gradient, and $|\cdot|$ the absolute value. It has been shown that ICOV allows for balanced and well localized edge strength measurements in bright regions as well as in dark regions of speckled imagery.

APPENDIX B: SPECKLE REDUCING ANISOTROPIC DIFFUSION (SRAD)

The SRAD algorithm is a partial differential equation (PDE) approach to speckle removal for ultrasonic image enhancement. It smoothes the imagery and enhances edges by inhibiting diffusion across edges and allowing isotropic diffusion on an intra-region basis. For images containing signal-dependent, spatially correlated multiplicative noise, SRAD excels over the adaptive speckle filters and conventional anisotropic diffusion techniques designed with additive noise models in mind.

Given an intensity image $I_0(x,y)$ having no zero points over the image domain Ω, the output image $I(x,y;t)$ is evolved according to the following PDE:

$$\partial I(x,y;t)/\partial t = \mathrm{div}[c(q)\,\nabla I(x,y;t)],$$

$$I(x,y;0) = I_0(x,y), \quad (\partial I(x,y;t)/\partial \vec{n})|_{\partial\Omega} = 0,$$

where ∇ is the gradient operator, div the divergence operator, $\partial\Omega$ denotes the border of Ω, $\vec{n}$ is the outer normal to the $\partial\Omega$, and the diffusion coefficient is given by

$$c(q) = \left\{ 1 + \frac{[q^2(x,y;t) - q_0^2(t)]}{q_0^2(t)(1+q_0^2(t))} \right\}^{-1},$$

where $q(x,y;t)$ is the instantaneous coefficient of variation as determined by (1), and $q_0(t)$ is the coefficient of variation measured in homogeneous speckle at instant t.

APPENDIX C: DECOMPRESSION OF LOG-COMPRESSED DATA

Specifically, the value of D can be determined iteratively by minimizing the Euclidean distance between a set of normalized moments computed using decompressed data and the corresponding theoretical speckle moments for fully developed speckle. For instance, assuming an arbitrary value for D, we compute a set of normalized moments, $\langle I_d^n \rangle / \langle I_d \rangle^n$ where $n=0.25$, 0.5, 1.5, 2, 2.5, and 3, over a homogeneous speckle region in the decompressed image $I_d = I_d(D)$. On the other hand, the theoretical nth normalized moment of fully developed speckle in intensity image is factorial n. Thus, we can choose the value of D^* according to

$$D^* = \arg\min_D \sum_{n \in S} [\langle I_d^n \rangle_i / \langle I_d \rangle_i^n - n\,!\,]^2,$$

where $S = \{0.25, 0.5, 1.5, 2, 2.5, 3\}$.

[a]Author to whom correspondence should be addressed. Janelle A. Molloy, Ph.D., Department of Radiation Oncology, Medical Center Box 800375, University of Virginia Health System, Charlottesville, VA 22908. Telephone: (434) 924-9423; Fax: (434) 982-3520; electronic mail: jam2y@virginia.edu

[1]A. Fenster, K. Surry, W. Smith, J. Gill, and D. B. Downey, "3D ultrasound imaging: Applications in image-guided therapy and biopsy," Comput. Graphics **26**, 557–568 (2002).
[2]Y. Yu and S. T. Acton, "Speckle reducing anisotropic diffusion," IEEE Trans. Image Process. **11**, 1260–1270 (2002).
[3]Y. Yu and S. T. Acton, "Edge detection in ultrasound imagery using the instantaneous coefficient of variation," IEEE Trans. Image Process. (to be published).
[4]Y. Yu and S. T. Acton, "Active contours with area-weighted binary flow for segmenting low SNR imagery," *Proceedings of International Conference on Image Processing*, **I** 129–132 Barcelona, Spain, September (2003).
[5]H. M. Ladak, F. Mao, Y. Wang, D. Downey, D. Steinman, and A. Fenster, "Prostate boundary segmentation from 2D ultrasound images," Med. Phys. **27**, 1777–1788 (2000).
[6]J. S. Prater and W. D. Richard, "Segmenting ultrasound images of the prostate using neural networks," Ultrason. Imaging **14**, 159–185 (1992).
[7]W. D. Richard and C. D. Keen, "Automated texture-based segmentation of ultrasound images of the prostate," Comput. Med. Imaging Graph. **20**, 131–140 (1996).
[8]Y. J. Liu, W. S. Ng, M. Y. Teo, and H. C. Lim, "Computerized prostate boundary estimation of ultrasound images using radial bas-relief method," Med. Biol. Eng. Comput. **35**, 445–454 (1997).
[9]C. K. Kwoh, M. Y. Teo, W. S. Ng, S. N. Tan, and L. M. Jones, "Outlining the prostate boundary using the harmonics method," Med. Biol. Eng. Comput. **36**, 768–771 (1998).
[10]S. D. Pathak, V. Chalana, D. R. Haynor, and Yongmin Kim, "Edge-guided boundary in prostate ultrasound images," IEEE Trans. Image Process. **19**, 1211–1219 (2000).
[11]R. G. Aarnink *et al.*, "A practical clinical method for contour determination in ultrasonographic prostate images," Ultrasound Med. Biol. **20**, 705–717 (1994).
[12]R. G. Aarnink *et al.*, "Edge detection in prostatic ultrasound images using integrated edge maps," Ultrasonics **36**, 635–642 (1998).
[13]F. A. Cosío and B. L. Davies, "Automated prostate recognition: A key process for clinically effective robotic prostatectomy," Med. Biol. Eng. Comput. **37**, 236–243 (1999).
[14]S. Lobregt and M. A. Viergever, "A discrete dynamic contour model," IEEE Trans. Med. Imaging **14**, 12–24 (1995).
[15]Y. Wang, H. N. Cardinal, D. B. Downey, and A. Fenster, "Semiautomatic three-dimensional segmentation of the prostate using two-dimensional ultrasound images," Med. Phys. **30**, 887–897 (2003).
[16]N. Hu, D. B. Downey, A. Fenster, and H. M. Ladak, "Prostate boundary segmentation from 3D ultrasound images," Med. Phys. **30**, 1648–1659 (2003).
[17]M. Kass, A. Witkin, and D. Terzopoulos, "Snakes: Active contour models," Int. J. Comput. Vis. **1**, 321–331 (1988).
[18]C. Knoll, M. Alcaniz, V. Grau, C. Monserrate, and M. C. Juan, "Outlining of the prostate using snakes with shape restrictions based on wavelet transform," Pattern Recogn. **32**, 1767–1781 (1999).
[19]T. Chan and L. A. Vese, "Active contours without edges," IEEE Trans. Image Process. **10**, 266–277 (2001).
[20]A. Yezzi, S. Kichenassamy, A. Kumar, P. Olver, and A. Tannenbaum, "A geometric snake model for segmentation of medical imagery," IEEE Trans. Med. Imaging **16**, 199–209 (1997).
[21]A. Yezzi, J. A. Tsai, and A. Willsky, "A statistical approach to snakes for bimodal and trimodal imagery," *Proceedings of ICCV*, 898–903, September (1999).
[22]S. Osher and J. A. Sethian, "Fronts propagating with curvature dependent speed: Algorithms based on Hamilton-Jocobi formulation," J. Comput. Phys. **79**, 12–49 (1988).
[23]A. Tsai, A. Yezzi, Jr., W. Wells, C. Tempany, D. Tucker, A. Fan, W. E. Crimson, and A. Willsky, "A shape based approach to the segmentation of medical imagery using level sets," IEEE Trans. Med. Imaging **22**, 137–154 (2003).
[24]C. Xu and J. L. Prince, "Snakes, shapes, and gradient vector flow," IEEE Trans. Image Process. **7**, 359–369 (1998).
[25]S. Egawa, T. M. Wheeler, D. R. Greene, and P. T. Scardino, "Unusual hyperechoic appearance of prostate cancer on transrectal ultrasonography," Br. J. Urol. **69**, 169–174 (1992).